

Article

# Investigations of MgO on Sintering Performance and Metallurgical Property of High-Chromium Vanadium-Titanium Magnetite

Liheng Zhang <sup>1</sup>, Songtao Yang <sup>2</sup>, Weidong Tang <sup>1</sup> and Xiangxin Xue <sup>1,\*</sup>

<sup>1</sup> School of Metallurgy, Northeastern University, Shenyang 110819, China; zhanglihengchn@gmail.com (L.Z.); tangwderos@163.com (W.T.)

<sup>2</sup> School of Material and Metallurgy, University of Science and Technology Liaoning, Anshan 114051, China; yangsongtao1984@163.com

\* Correspondence: xuexx@mail.neu.edu.cn; Tel.: +86-24-83687719

Received: 6 May 2019; Accepted: 21 May 2019; Published: 27 May 2019



**Abstract:** High-chromium vanadium-titanium magnetite (HCVTM) in the Hongge region has been used as an essential mineral resource in ironmaking. The effects of MgO on sintering performance and metallurgical properties were investigated by sintering pot tests, X-ray diffraction (XRD), and scanning electron microscopy-energy dispersive spectroscopy (SEM-EDS). HCVTM sinters with varying MgO contents (2.7–3.5%), which was achieved by adding dolomite, were tested for yield, strength, reduction degradation index (RDI), reduction index (RI), and softening-melting properties. The productivity and the comprehensive index were evaluated. The results show that yield and productivity increased, while the vertical sintering speed and the tumbler index (TI) initially increased then decreased with the increase of MgO content. The mineral structure of HCVTM sinter changed from a non-uniform state to a uniform state with increased MgO content. Most of the Mg<sup>2+</sup> entered the magnetite lattice, while a small amount entered the perovskite and the calcium silicate. The increase of MgO content improved RDI and softening-melting properties while reducing RI. The best recommended amount of MgO was 3.3% from the comprehensive index.

**Keywords:** MgO; high-chromium vanadium-titanium magnetite; sintering pot test; sintering performance; metallurgical property

## 1. Introduction

In recent years, a kind of high-chromium vanadium-titanium magnetite (HCVTM) was discovered in Hongge district, Sichuan Province, and the reserve exceeded 3.5 billion tons. HCVTM containing valuable elements (Fe, Ti, Cr, V) can satisfy the requirement of Ti, Cr, and V metal as well as their alloys given the exploitation of ilmenite and chromite minerals [1,2]. HCVTM has a high content of valuable elements, which shows a comprehensive utilization value. At present, the blast furnace (BF) charge structure is mainly composed of high alkalinity sinter, acid pellets, and massive minerals [3]. Due to the insufficient supply of pellets and massive high-grade minerals in China, the reserves of vanadium-titanium magnetite in the southwestern region are enough, and it is necessary and meaningful to conduct comprehensive utilization research on HCVTM sintered ore [4,5]. Hence, high basicity sinter can be used as the main feedstock during ironmaking operation processes, and the valuable elements such as Ti, Cr, and V can be extracted from BF slag and vanadium slag [6–10].

Production of rich-containing MgO sinter has become an effective way to solve problems such as the high viscosity and low desulfurization ability of the slag that is brought by large-scale use of high-titanium iron ores in BF [11–16]. The BF slag properties can be improved with properly increased MgO content of sinter in the BF, and then the improved properties of slag could be conducive to the

techno-economic indices of the BF [17,18]. However, the high MgO content decreases the quantity of the bonding phase during the sintering process and leads to low sinter strength. The effects of mineralogy on the physical and the metallurgical properties of sinter were studied by Umadevi [19]. The addition of Mg-bearing materials in sinter affected the microstructure and the chemical properties of sinter. Moreover, the increased MgO content was able to reduce the sinter strength due to the generation of a glass phase, which could suppress the formation of calcium ferrite according to Yadav's study [15]. Gan et al. [20] reported that the increased MgO content improved the properties of sinter, and the suitable MgO content was less than 3.7% in titaniferous magnetite sinter. The influence and the mechanism of MgO on the strength of high basicity sinter were studied by Fan et al. [21]. The mechanism study shows that, as the MgO content increased, the liquidus temperature of the sintered mixture increased, and the liquid fraction decreased. Yang et al. [18] found that the proper MgO content in chromium-bearing vanadium-titanium magnetite in the Chengde area was 3.56%. Furthermore, the above studies were based on ordinary iron ore sinter or some titaniferous magnetite sinter. The effects of MgO on the characteristics of Ti, Cr, and V-bearing mineral phases as well as on the reduction and the softening-melting properties have not been studied and elaborated in detail.

In this paper, the MgO content was dependent on the addition of dolomite. The comprehensive index was calculated to obtain a suitable range of MgO additive. The sintering performance and the metallurgy property of HCVTM sinter were investigated with the increase of MgO content, and the mechanism of MgO influencing mineral compositions and sinter quality was revealed.

## 2. Experiment

### 2.1. Materials Analysis and Characteristic

The HCVTM iron ore was from the Hongge region (Panzhuhua, China), and the ordinary magnetite, gas-ash, magnetic powder, lime, coke, and coal were provided by Chengde Jianlong Iron and Steel Group Company (Hebei, China). The chemical compositions of raw materials and flue are shown in Tables 1 and 2, respectively.

**Table 1.** The chemical compositions of raw materials (wt %).

Raw Materials	TFe	FeO	TiO <sub>2</sub>	V <sub>2</sub> O <sub>5</sub>	Cr <sub>2</sub> O <sub>3</sub>	CaO	SiO <sub>2</sub>	MgO	Al <sub>2</sub> O <sub>3</sub>	P	S
HCVTM *	56.45	28.05	11.01	1.32	0.55	0.63	2.66	2.54	2.42	0.01	0.34
Gas-ash	32.39		1.79	0.25	0.16	5.16	5.95	1.79	2.69	0.07	0.17
Magnetic powder	0.14		0.03			29.4	2.58	20.65	0.90		
Ordinary Magnetite	63.79	28.35	0.89	0.06	0.02	0.38	7.15	0.38	1.25	0.02	0.05
Dolomite						28.97	7.77	20.2	1.16		
Quicklime						60.80	3.42	2.87	1.11		

\*: high-chromium vanadium-titanium magnetite.

**Table 2.** Industrial analysis and chemical compositions of the fuel (wt %).

Item	Fixed Carbon	Volatile	Organic Compounds	Ash					Σ
				CaO	SiO <sub>2</sub>	MgO	Al <sub>2</sub> O <sub>3</sub>	others	
Coke	76.90	0.559	1.48	1.35	6.4	0.28	4.18	8.85	100.00
Coal	85.40	0.147	1.35	0.74	4.6	0.18	3.35	4.23	100.00

Figure 1 presents the scanning electron microscopy (SEM) micrographs of the HCVTM particles. The shape of the HCVTM particles was heterogeneous and angular. The energy dispersive spectroscopy (EDS) point analysis of the HCVTM particles at different regions was performed, and the results are as shown in Table 3. According to the EDS point analysis results, points A and B contained an abundant amount of Fe, O, Ti, and little Si, Al, Mg, V, and Cr, and therefore could be inferred as titanomagnetite.

However, point C mainly contained Si, Al, Mg and O. Thus, it was identified as magnesium aluminate spinel, which is darker than other particles due to it containing silicon. Figure 2 shows the X-ray diffraction (XRD) pattern of the HCVTM. It can be seen that the main phases of the HCVTM were magnetite, ilmenite, chromium spinal, and vanadium spinal.

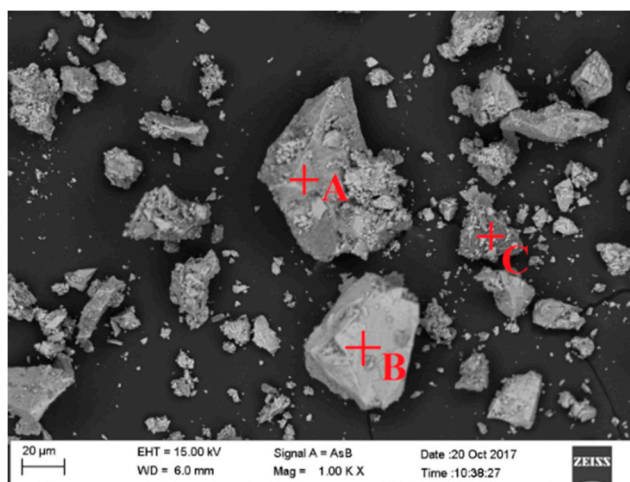


Figure 1. Micrographs of typical HCVTM particles.

Table 3. Elemental composition of grain mark in Figure 1 (wt %).

Point	Fe	Si	Al	Mg	Ti	V	Cr	O
A	69.88	0.39	0.54	0.54	16.54	0.59	0.42	11.09
B	38.21	-	-	1.38	34.38	0.26	0.43	25.34
C	-	14.83	12.77	20.86	-	-	-	51.54

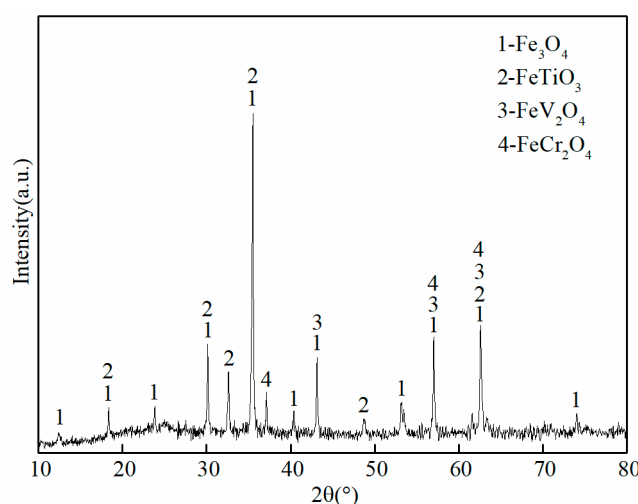


Figure 2. XRD pattern of the HCVTM.

## 2.2. Sinter Pot Test

The experimental scheme is shown in Table 4. The MgO content increased from 2.7% to 3.5% by changing the dolomite addition. The experimental procedure of the sinter pot test contained burdening, mixture, pelletizing, ignition, sintering, cooling, and crushing disposal [22]. The operation parameters of the sinter pot test are shown in Table 5. The sinter pot test was finished at the end of the gas temperature when it reached the peak value. Then, the sinter was cooled by air for 10 min and poured out to crush. The crushed sinter was dropped from a height of 2 m three times and sieved into five

particle sizes as follows: less than 5 mm, between 5 to 10 mm, between 10 to 25 mm, between 25 to 40 mm, and more than 40 mm.

**Table 4.** Experimental scheme and ingredient of sinter materials.

Number	$\omega(\text{MgO})/\%$	Mixed Sinter Raw Materials (100 %)/wt %							CaO/SiO <sub>2</sub>	$\omega(\text{C})/\%$
		HCVTM	Magnetite	Return Mine	Gas Ash	Magnetic Powder	Quick-Lime	Dolo-Mite		
1	2.7	35.0	30	20	1	1	11.6	1.5	1.9	5.0
2	2.9	34.2	30	20	1	1	11.3	2.5	1.9	5.0
3	3.1	33.1	30	20	1	1	11.3	3.6	1.9	5.0
4	3.3	32.8	30	20	1	1	10.5	4.7	1.9	5.0
5	3.5	32.2	30	20	1	1	10.1	5.7	1.9	5.0

**Table 5.** Parameters of HCVTM sintering pot test.

Item	Parameter	Item	Parameter
Sinter pot height	700 mm	Sinter pot inner diameter	320 mm
Sintering weight	100 kg	Pelletizing time	10 min
Ignition temperature	1050 °C	Ignition time	2 min
Ignition pressure	8.0 kPa	Exhausting pressure	12.0 kPa

### 2.3. Definition of Parameters

#### 2.3.1. Vertical Sintering Speed

The vertical sintering speed (VSS) is an index to indicate the sintering rate. The calculation equation of VSS is given in Equation (1):

$$VSS = \frac{L}{T} \quad (1)$$

where  $L$  is the thickness of the raw material (mm), and  $T$  is the sintering time (min).

#### 2.3.2. Productivity

The productivity [23] was calculated using the following Equation (2):

$$P = M_S \times y / (A \times t) \quad (2)$$

where  $P$  is the unit productivity ( $\text{t} \cdot \text{m}^{-2} \cdot \text{h}^{-2}$ ),  $M_S$  is the mass of sinter cake (t),  $y$  is the yield of product sinter (%),  $A$  is the cross-section area of the sinter pot ( $\text{m}^2$ ), and  $t$  is the sintering time (h).

#### 2.3.3. Reduction Degradation Index

The reduction degradation index (RDI) is a measure of the disintegration property of sinter upon exposure to CO at 500 °C according to the standard of ISO-4696. The equations of RDI are given in Equations (3)–(5):

$$RDI_{+6.3} = \frac{m_{D1}}{m_{D0}} \times 100 \quad (3)$$

$$RDI_{+3.15} = \frac{m_{D1} + m_{D2}}{m_{D0}} \times 100 \quad (4)$$

$$RDI_{-0.5} = \frac{m_{D0} - (m_{D1} + m_{D2} + m_{D3})}{m_{D0}} \times 100 \quad (5)$$

where  $m_{D0}$  is the sinter weight after the reduction (g),  $m_{D1}$  is the weight of the sinter on the 6.3 mm sieve (g),  $m_{D2}$  is the weight of the sinter on the 3.15 mm sieve (g), and  $m_{D3}$  is the weight of the sinter on the 0.5 mm sieve (g).

### 2.3.4. Reduction Index

The reduction index (RI) is determined by the ISO-7215 test performed at 900 °C. The equations of RDI are given in Equation (6):

$$X_t = \left[ \frac{0.11\omega(\text{FeO})}{0.43\omega(\text{TFe})} + \frac{m_1 - m_2}{m_1 \times 0.43\omega(\text{TFe})} \right] \times 100\% \quad (6)$$

where  $X_t$  is the RI of the HCVTM sinter at time  $t$  (%),  $\omega(\text{FeO})$  and  $\omega(\text{TFe})$  are the mass of FeO and the total ferrous of the HCVTM sinter before reduction (%), and  $m_1$  and  $m_2$  are the masses of the HCVTM sinter before reduction (g).

### 2.3.5. Softening-Melting Properties

The softening-melting properties of sinter have a significant effect on the reduction process and the permeability of the load. In this work, softening start temperature ( $T_{10\%}$ ) and softening end temperature ( $T_{40\%}$ ) are the burden temperatures when shrinkage degrees reach 10% and 40%, respectively. The melting start temperature ( $T_S$ ) is the temperature that the gas pressure drop begins to increase rapidly. The melting end temperature ( $T_D$ ) is the dripping temperature of iron. The softening zone of sinter is the softening temperature interval ( $\Delta T_1 = T_{40\%} - T_{10\%}$ ). The melting zone of sinter is the melting temperature interval ( $\Delta T_2 = T_D - T_S$ ).

A characteristic value  $S$  is introduced to evaluate the dripping performance of the sinter. The smaller the  $S$  is, the better the droplet performance will be. The equation of  $S$  is given in Equation (7):

$$S = \int_{t_S}^{t_D} (\Delta P_m - \Delta P_s) \cdot dt \quad (7)$$

where the  $\Delta P_s$  is the starting melting pressure difference, the value of which is  $50 \times 9.8$  Pa, and  $\Delta P_m$  is the maximum pressure difference, Pa.

## 3. Results and Discussion

### 3.1. Sintering Performance

As shown in Figure 3, with increased MgO content, the VSS calculated by Equation (1) increased firstly and then decreased when the MgO content reached 3.3%. In the process of granulation, the pelletizing property of the raw material mixture and the strength of the pelletized sinter materials were improved due to the higher cohesiveness of dolomite compared with lime. The addition of dolomite reduced the permeability of the pelletized sinter materials. This change decreased the sinter resistance and increased the sintering rate. At the same time, compared with other fluxes, magnesium-containing minerals were less likely to undergo an assimilation reaction. MgO and SiO<sub>2</sub> could form a melt at a temperature higher than 1350 °C, and they could form a melt with Fe<sub>2</sub>O<sub>3</sub> higher than 1600 °C. The increase in dolomite increased the liquid-phase formation temperature, resulting in a decrease in the sintering speed.

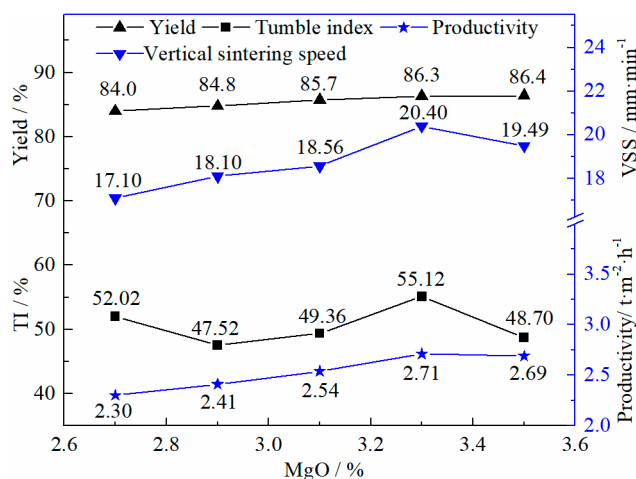


Figure 3. Sinter properties of HTCVM sinters with different MgO contents.

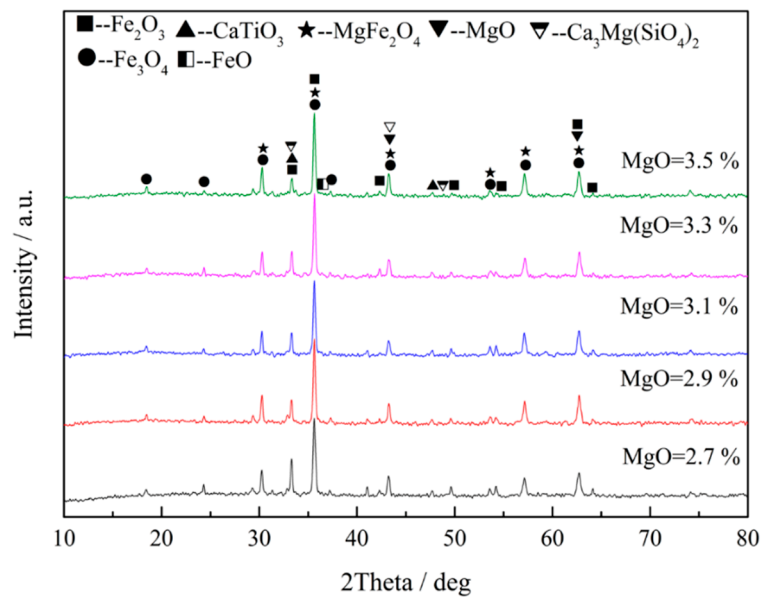
The yield and the productivity of the HCVTM sinter mainly increased with increased MgO content, which indicated the positive effect of dolomite addition on the HCVTM sinter. The addition of MgO hurt the formation of calcium ferrite, but it could contribute to the formation of silicate and magnetite to stabilize the conglomeration of magnetite. In areas with high local MgO content, the glass phase content was reduced, which was beneficial to increasing the sinter strength. The productivity was calculated using Equation (2). During HCVTM sintering,  $y$  and  $t$  changed simultaneously with the increase of MgO content, but their changing rates were different. After calculation, the trend of productivity increased.

Figure 3 shows the tumbler index (TI) firstly increased and then decreased with increased MgO content. The maximum TI was 55.12% when the MgO content was 3.3%. With increased MgO content from 2.7% to 3.3%, the TI improved because the crystal intensity of the sinter was strengthened by the increased hematite content and the refined mineral grains. When the MgO content increased to 3.5%, the magnetite covered hematite structure reduced the sinter strength. Yang [18] considered that silicate and glass phases had important effects on bonding phases, and TI improved with increased Mg-bearing silicate and a decreased glass phase. A.D. Pelton and G. Trömel [24,25] studied Mg-bearing mineral phases and determined they had a high melting point and high strength; hence, the sinter strength improved with increased Mg-bearing phases.

### 3.2. Mineral Composition and Microstructure

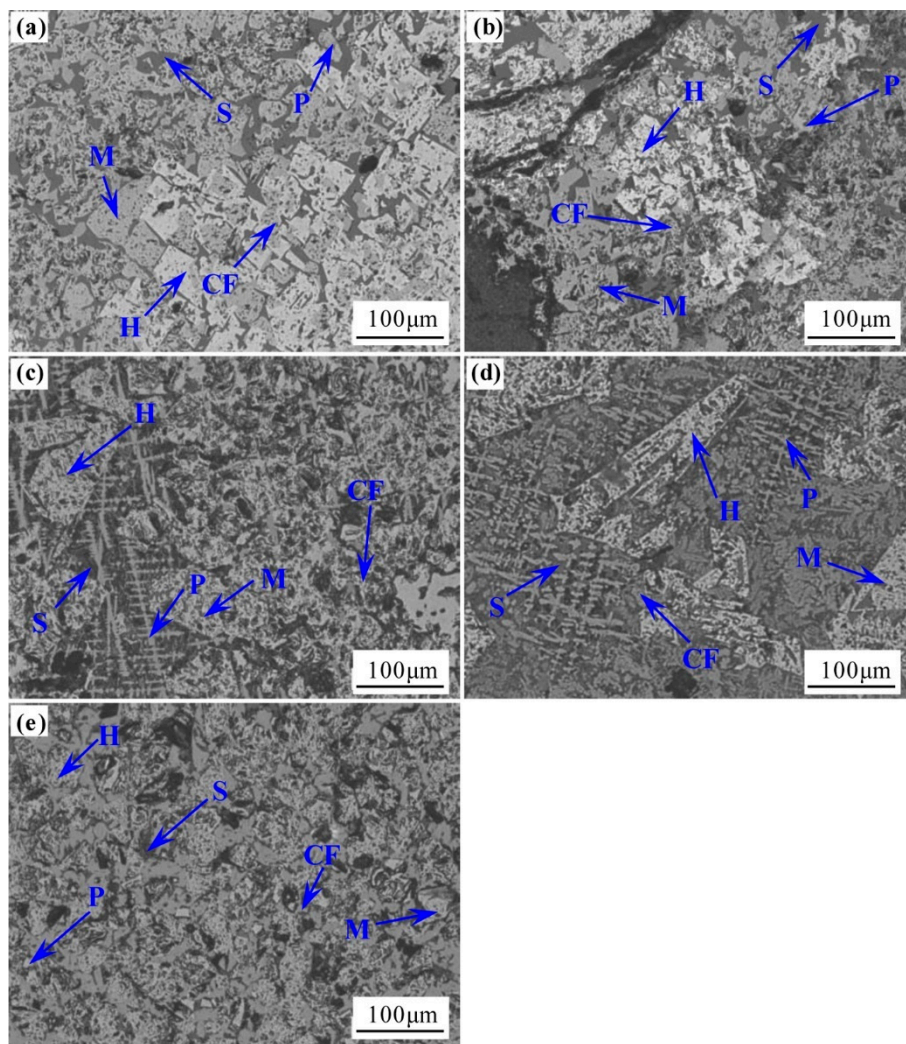
According to the analysis of the XRD pattern of the HCVTM sinter with different MgO contents (Figure 4), the main phases of the HCVTM sinter were magnetite ( $\text{Fe}_3\text{O}_4$ ), hematite ( $\text{Fe}_2\text{O}_3$ ), perovskite ( $\text{CaTiO}_3$ ), and magnesium ferrite ( $\text{MgFe}_2\text{O}_4$ ). Changing the MgO content was the reason for the diverse mineral compositions. The following reactions (8)–(10) could be suggested in the sintering process:





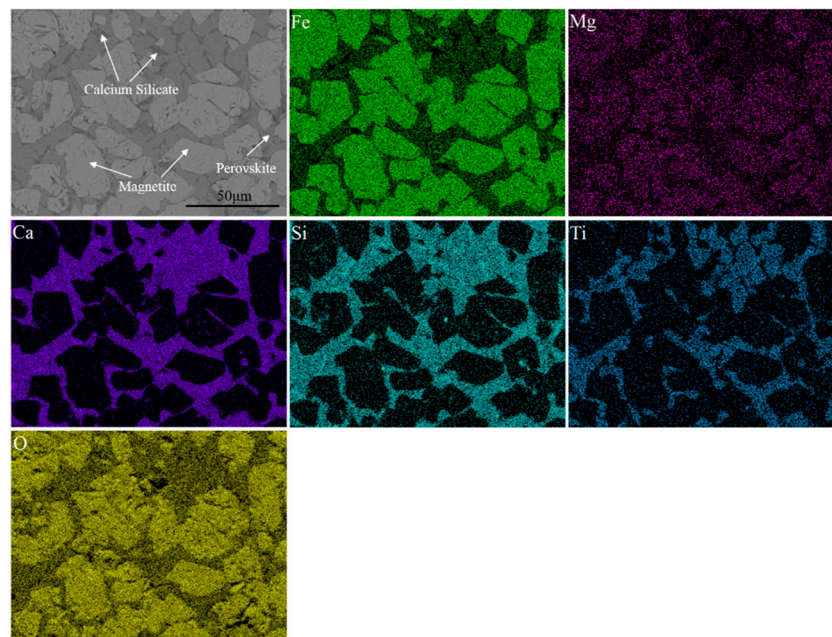
**Figure 4.** XRD pattern of HCVTM with different mass-% MgO.

Figure 5 shows the microstructure of the HCVTM sinters with different MgO contents ranging from 2.7% to 3.5%. The mineral structure of the HCVTM sinter changed from a non-uniform state to a uniform state with increased MgO content. Figure 5a shows the mineral phases, including the large hematite grain, the small magnetite grain, the perovskite, and the calcium ferrite (CF). With MgO content increased to 2.9% (Figure 5b), the main mineral phases were euhedral magnetite grains. Subhedral perovskite and anhedral perovskite filled in the intervals of other mineral phases. The surface of the magnetite was covered by hematite, and this structure had structure stress, which was harmful to the sinter structure. When the MgO content increased from 3.1% to 3.3% (Figure 5c,d), the large hematite and magnetite grains were refined to small grains, and secondary skeleton hematite phases were generated around the magnetite. Dendritic perovskite, acicular, and schistose CF phases were distributed in the silicate phase. When the MgO content increased to 3.5% (Figure 5e), the magnetite grains became smaller due to the reaction between MgO and  $\text{Fe}_3\text{O}_4$ . The distribution of the magnetite and the silicate phases was non-uniform; perovskite distributed on the boundary of the silicate phases, and the structure was harmful to the sinter structure. Panigrahy [26] revealed that the increase of MgO content suppressed the formation of hematite and Ca-ferrite phases while increasing the magnetite phase. The perovskite increased, while the CF decreased in the silicate bonding phase. Furthermore, the distribution of the mineral phase became more uniform compared with the HCVTM sinter with low MgO content.



**Figure 5.** Microstructure of HCVTM sinter with different MgO content. M: magnetite; H: hematite; P: perovskite; CF: calcium ferrite; S: silicate. (a) MgO = 2.7%; (b) MgO = 2.9%; (c) MgO = 3.1%; (d) MgO = 3.3%; (e) MgO = 3.5%.

The distribution of MgO in different phases of the sinter could have been considered as an important factor due to its influence on sinter strength and structure. Previous research has reached very different conclusions on the subsequent distribution of MgO in different phases of sinter structure. While Long [27] indicated that MgO was distributed to the silicate forming akermanite and calcium-magnesium olivine in the sinter structure, Zhou [28] found that most of the  $Mg^{2+}$  entered the magnetite lattice to form magnesiospinels of the type  $(Fe, Mg)O \cdot Fe_2O_3$  by displacing  $Fe^{2+}$  ions from the magnetite lattice, and a small amount was partitioned to glass and calcium silicate. To better understand the distribution of MgO in different sinter phases in this study, some SEM-EDS mapping analysis was performed for different phases. Figure 6 shows an example of the difference in the distribution of Mg and other elements in different phases, including magnetite, hematite, silicate, and perovskite. The results show that the Mg element was mainly distributed in the magnetite and the hematite phases, and it was negligible in the perovskite and the silicate phases.



**Figure 6.** SEM image and energy dispersive spectroscopy (EDS) mapping of the HCVTM sinter.

### 3.3. Metallurgical Property of HCVTM Sinter

Figure 7 shows the influence of MgO on the RDI calculated by Equations (3)–(5). The  $RDI_{+3.15}$  and the  $RDI_{+6.3}$  increased, while  $RDI_{-0.5}$  decreased with increased MgO content. There were two reasons for the improvement of the RDI. First, the rhombohedral hematite in HCVTM underwent crystal transformation during the reduction process, causing volume expansion and fragmentation [26]. The generation of the secondary skeleton hematite phase improved the reduction disintegration of the HCVTM sinter. Moreover, the titanohematite and the titanomagnetite were multicomponent solid solutions—they were not only solid solutions of  $TiO_2$ , but also solid solutions of  $Al_2O_3$ , MgO, and the like [20]. Due to their different crystal systems, solid solution elements, contents, and expansion coefficients, the stresses and the directions generated during the reduction were diverse, which caused reduction cracks in the sintered ore and quickly formed a network of fractured bands (Figure 8a). The  $RDI_{+3.15}$  increased to 86.4% with 3.5% MgO addition, and the reason was that the reduction disintegration was restrained because the hard-reduced magnetite phase reacted with MgO to form a magnetite solid solution  $((Fe, Mg)O \cdot Fe_2O_3)$ . Yang [18] and Zhou [28] all considered that the RDI of sinter would increase when the MgO content increased due to the increase of magnetite and Mg-bearing phases with a lower reduction index. Second,  $TiO_2$  and  $Al_2O_3$ , which were dissolved in the silicate phases, including the glass phase and the titanium garnet, could significantly destroy the fracture toughness [20]. In the titanium garnet accumulation area, especially the large-grain titanium garnet accumulation area, there were coarse cracks, which were further expanded by the stress during the reduction process to cause the sinter to be pulverized (Figure 8b). With the increase of MgO content, the formation of coarse triangular and incomplete quadrilateral titanium hematite was reduced, the sintered ore formed a microporous thick-wall structure, and the strength was improved. Meanwhile, since MgO could improve the crystallization ability of the silicate melt and reduce the vitreous content, the forsterite and the pyroxene  $(Ca(Mg,Fe)Si_2O_5)$  minerals precipitated in the glass phase acted as a skeleton, which enhanced the ability to withstand stress changes and crack propagation. Therefore, as the MgO content increased, the reduction crack of the sinter decreased and became smaller, thus that the pulverization rate decreased.

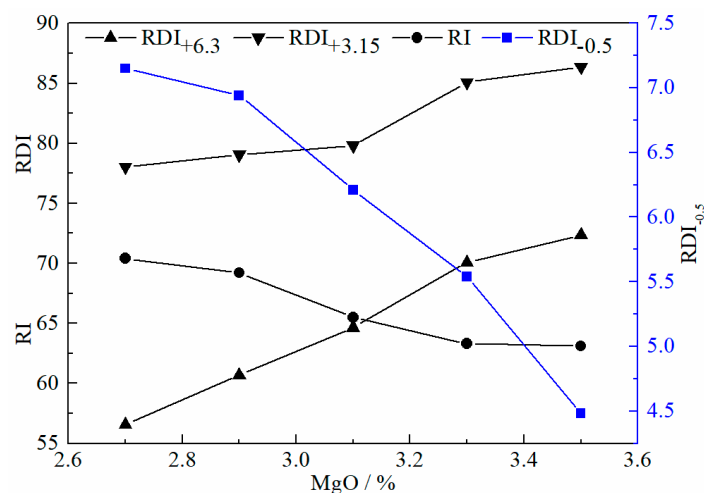


**Figure 7.** Reduction degradation index (RDI) and reduction index (RI) of the HTCVM sinters with different MgO contents.

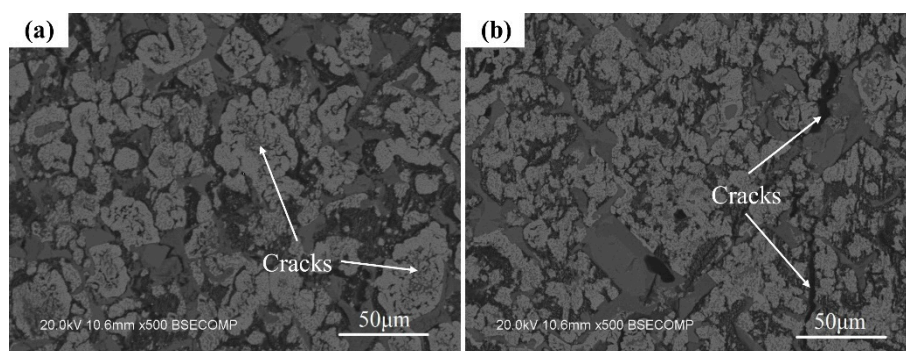


**Figure 8.** Microstructure after low temperature reduction (a) 2.7% MgO; (b) 2.9% MgO.

With the increase of MgO content, the RI calculated by Equation (6) decreased from 70.4% to 63.1% (Figure 7). Moreover, the FeO content decreased from 21.22% to 13.86%. The reduction of iron oxides was restrained due to the refractory minerals with increased MgO content [18]. When MgO was dissolved in magnetite, it promoted the stable existence of difficult-reducing magnetite and gradually reduced the easily reduced titanium hematite. At the same time, with the increase of MgO, minerals such as calcium-magnesium olivine (difficult to reduce) were formed. These minerals formed an aerobic interweaving structure with magnetite and calcium ferrite, which made the sintered ore denser and more difficult to reduce.

Figure 9 shows the softening-melting properties of the HCVTM sinter with different MgO contents.  $T_{10\%}$  increased from 1106 °C to 1119 °C, and  $T_{40\%}$  increased from 1178 °C to 1182 °C with the increased MgO content.  $\Delta T_1$  increased from 72 °C to 63 °C.  $T_S$  increased from 1222 °C to 1234 °C, and  $T_D$  decreased from 1428 °C to 1443 °C with the increased of MgO content.  $\Delta T_2$  increased from 206 °C to 209 °C.

For smelting of the sinter in the BF, a high  $T_{10\%}$  and an applicable scale of  $\Delta T_1$  were beneficial to the reduction reactions of iron ore [29]. Hence, the HCVTM sinter had a better tendency regarding the softening behavior with increased MgO content. The increased MgO content led to the increase of high melting point minerals such as magnesium magnetite and calcium forsterite in the sintering process, which was the reason for the increase of  $T_{10\%}$  and  $T_{40\%}$ .  $T_S$  increased with the decrease of FeO content and the increase of the high-melting liquid phase. The  $T_D$  depended on the melting point of the slag phase and the metal carburizing reaction. With the decreased FeO and decreased RI, the  $T_D$  increased.

Figure 10 presents the indices, including maximum differential pressure ( $\Delta P_m$ ) and gas permeability index (S). The gas pressure difference ( $\Delta P_m$ ) decreased from 9.9 kPa to 8.1 kPa. In general, the S value

of the softening-melting property of sinter is mainly used to evaluate the gas permeability index of sinter. The smaller the S value is, the better the gas permeability index of sinter will be. According to Equation (7), the S decreased from 1938 kPa·°C to 1613 kPa·°C due to the drastic decrease of  $\Delta P_m$  and a slight increase of  $\Delta T_2$ , which indicated that the sinter softening-melting properties were improved with the increased MgO content [30].

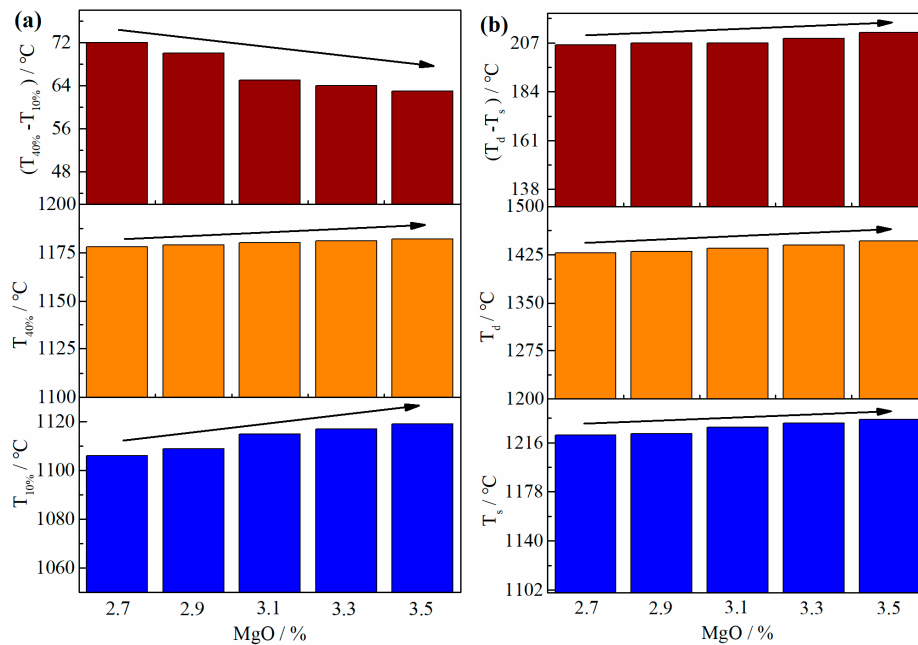


Figure 9. The softening-melting properties of the HCVTM sinter with different MgO contents (a) softening property; (b) melting property.

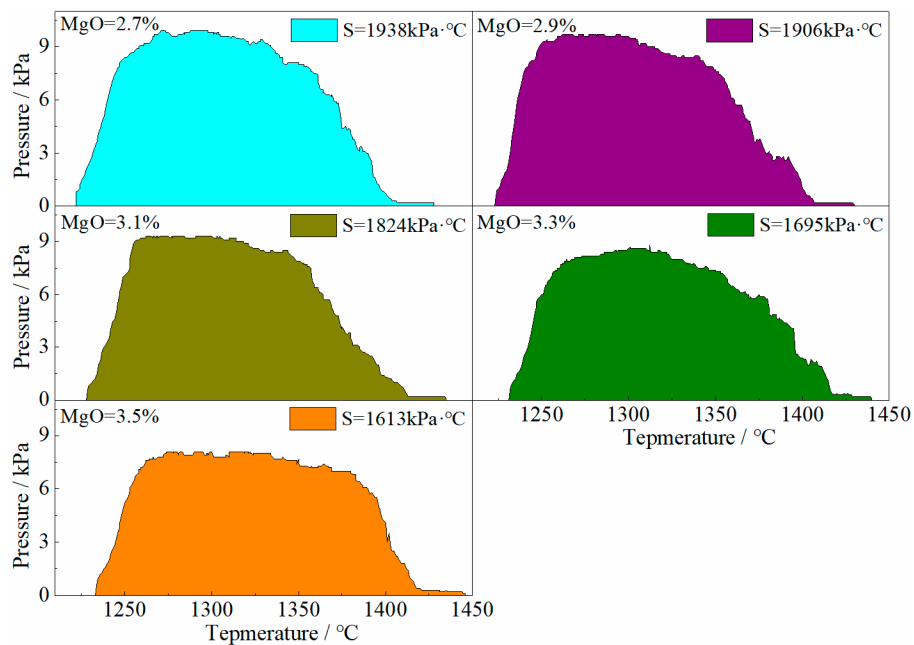


Figure 10. The gas permeability of the HCVTM sinter with different MgO contents.

### 3.4. Comprehensive Index

When sintering rate, yield, productivity, TI, RDI, and RI achieved optimum performance, the corresponding MgO content was different. Therefore, the composite index [28] was used to find the most suitable MgO content.

The first set of composite indices was set as a reference and quantified to 100 for comparison and analysis. Based on years of experience in the production of vanadium-titanium magnetite, Jianlong Steel determined the selected indicators (sintering rate, yield, strength, RDI, and RI) and the significance coefficient. The total significance coefficient was 100, and sintering rate, yield, productivity, TI, RDI, and RI significant coefficients were 5, 25, 10, 20, 20, and 20, respectively.

Define:

$$R_j = (z_{ij})_{max} - (z_{ij})_{min} \quad (11)$$

where  $R_j$  is the range,  $z_{i1}$  is VSS,  $z_{i2}$  is productivity,  $z_{i3}$  is yield,  $z_{i4}$  is TI,  $z_{i4}$  is RDI, and  $z_{i5}$  is RI.

$$w_j = W_j R_j \quad (12)$$

where  $w_j$  is the unit range coefficient, and  $W_j$  is the significant coefficient.

$$f_i = \sum_{j=1}^m w_j z_{ij} (i = 1, 2, \dots, m) \quad (13)$$

$$F_i = f_i - f_1 + 100 \quad (14)$$

where  $F_i$  is the comprehensive index, and  $f_i$  is the composite index.

Table 6 shows the calculation process of the comprehensive index according to Equations (11)–(14). Figure 11 shows the comprehensive index. It can be seen that, as the MgO content increased from 2.7% to 3.3%, the comprehensive index increased from 100 to 145.21 and then decreased to 129.26 when MgO increased to 3.5%. From the comprehensive index, the best recommended amount of MgO was 3.3%.

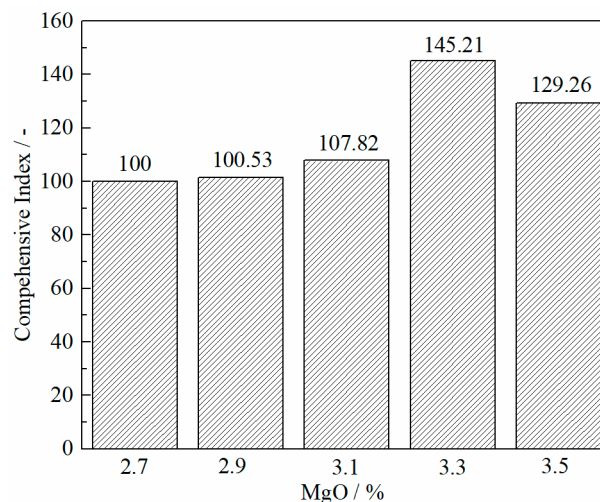


**Figure 11.** Effect of MgO content on comprehensive index of HCVTM.

**Table 6.** Calculation process of comprehensive index.

$\omega(\text{MgO})/\%$	$z_{i1}$	$z_{i2}$	$z_{i3}$	$z_{i4}$	$z_{i5}$	$z_{i6}$	$f_i$	$F_i = f_i - f_1 + 100$
2.7	17.10	2.30	84.00	52.02	78.02	70.4	1032.70	100
2.9	18.10	2.41	84.80	47.52	79.05	69.2	1034.24	101.53
3.1	18.56	2.54	85.70	49.36	79.82	65.5	1040.53	107.82
3.3	20.40	2.71	86.30	55.12	85.09	63.3	1077.91	145.21
3.5	19.88	2.69	86.40	48.70	86.38	63.1	1061.97	129.26
$R_j$	3.30	0.41	2.40	7.60	8.36	7.3		
$W_j$	5	25	10	20	20	20		
$\omega_j$	1.52	60.98	4.17	2.63	2.39	2.74		

#### 4. Conclusions

- (1) With MgO content increased from 2.7% to 3.5%, the yield and the productivity increased, while the VSS and the TI initially increased then decreased.
- (2) The mineral structure of the HCVTM sinter changed from a non-uniform state to a uniform state with increased MgO content. Most of the  $\text{Mg}^{2+}$  entered the magnetite lattice, while a small amount entered the perovskite and the calcium silicate.
- (3) With the increased MgO content, the RDI sinter increased while the RI decreased. Additionally, the sinter softening-melting properties were improved. According to the comprehensive index, the optimal recommended amount of MgO was 3.3%.

**Author Contributions:** Conceptualization, X.X. and L.Z.; methodology, S.Y.; software, W.T.; validation, X.X., L.Z. and S.Y.; formal analysis, X.X.; resources, X.X.; data curation, S.Y.; writing—original draft preparation, L.Z.; writing—review and editing, L.Z., W.T. and X.X.; project administration, X.X.; funding acquisition, X.X.

**Acknowledgments:** This work was financially supported by National Basic Research Program of China (973 Program) (No.2013CB632603), and the National Key Technology R&D Program (No. 2015BAB19B02), and National Natural Science Foundation of China (Nos. 51090384, 51174051 and 51574082), the Fundamental Research Funds for the Central Universities (No. N182503035).

**Conflicts of Interest:** The authors declare no conflict of interest.

#### References

1. Takano, C.; Zambrano, A.P.; Nogueira, A.E.A.; Mourao, M.B.; Iguchi, Y. Chromites reduction reaction mechanisms in carbon-chromites composite agglomerates at 1773K. *ISIJ Int.* **2007**, *47*, 1585–1589. [[CrossRef](#)]
2. Lu, C.; Zou, X.; Lu, X.; Xie, X.; Zheng, K.; Xiao, W.; Cheng, H.; Li, G. Reductive kinetics of Panzhihua ilmenite with hydrogen. *Trans. Nonferrous Met. Soc. China* **2016**, *26*, 3266–3273. [[CrossRef](#)]
3. Wu, S.; Xu, H.; Tian, Y. Evaluation of lump ores for use in modern blast furnaces as part of mixed burden practice. *Ironmak. Steelmak.* **2013**, *36*, 19–23. [[CrossRef](#)]
4. Liao, J.; Li, J.; Wang, X.; Zhang, Z. Influence of  $\text{TiO}_2$  and basicity on viscosity of Ti bearing slag. *Ironmak. Steelmak.* **2012**, *39*, 133–139. [[CrossRef](#)]
5. Zhang, L.; Zhang, L.; Wang, M.; Li, G.; Sui, Z. Dynamic oxidation of the Ti-bearing blast furnace slag. *ISIJ Int.* **2006**, *46*, 458–465. [[CrossRef](#)]
6. Moskalyk, R.; Alfantazi, A. Processing of vanadium: A review. *Miner. Eng.* **2003**, *16*, 793–805. [[CrossRef](#)]
7. Chen, D.; Song, B.; Wang, L.; Qi, T.; Wang, Y.; Wang, W. Solid state reduction of Panzhihua titanomagnetite concentrates with pulverized coal. *Miner. Eng.* **2011**, *24*, 864–869. [[CrossRef](#)]
8. Rocha, M.; Silva, A.; Mourao, M.; Kurauchi, M.; Takano, C. Fundamental aspects of sintering of chromites concentrates. *Miner. Process. Extr. M.* **2014**, *123*, 251–256. [[CrossRef](#)]
9. Zhang, G.; Zhang, T.; Lv, G.; Zhang, Y.; Liu, Y.; Gang, X. Extraction of vanadium from LD converter slag by pressure leaching process with titanium white waste acid. *Rare Metal Mat. Eng.* **2015**, *44*, 1894–1898.
10. Zhang, L.; Zhang, L.; Wang, M.; Li, G.; Sui, Z. Recovery of titanium compounds from molten Ti-bearing blast furnace slag under the dynamic oxidation condition. *Miner. Eng.* **2007**, *20*, 684–693. [[CrossRef](#)]

11. Li, Q.; Huang, Z.Z.; Jiang, T.; Yang, Y.B.; Li, G.H. Effect of dolomite and serpentine on sinter quality and microstructure. *Iron Steel* **2006**, *41*, 10–14.
12. Yu, S.R.; Yu, S.J.; Liu, Y.H.; Li, Y.M. Influence of MgO content on the sinter index and the metallurgical property. *Angang Technol.* **2008**, *353*, 23–26.
13. Zhou, M.S.; Li, Y.R. Laboratory study on reasonable MgO content in the sinter of Anshan iron and steel group co. *Sinter. Pelletizing* **2005**, *6*, 1–4.
14. Zhao, Z. Laboratory sintering study with adding dolomite fines. *Sinter Pelletizing* **2003**, *28*, 25–27.
15. Yadav, U.S.; Pandey, B.D.; Das, B.K.; Jene, D. Influence of magnesia on sintering characteristics of iron ore. *Ironmak. Steelmak.* **2002**, *29*, 91–95. [[CrossRef](#)]
16. Yang, L.X.; Davis, L. Assimilation and mineral formation during sintering for blends containing magnetite concentrate and hematite/pisolite sintering fines. *ISIJ Int.* **2007**, *39*, 239–245. [[CrossRef](#)]
17. Liu, Z.; Chu, M.; Wang, H.; Zhao, W.; Xue, X. Effect of MgO content in sinter on the softening-melting behavior of mixed burden made from chromium-bearing vanadium-titanium magnetite. *Int. J. Miner. Metall. Mater.* **2016**, *23*, 25–32. [[CrossRef](#)]
18. Yang, S.T.; Tang, W.D.; Zhou, M.; Jiang, T.; Xue, X.X.; Zhang, W.J. Effect of dolomite on mineral composition and metallurgical properties of chromium-bearing vanadium-titanium magnetite sinter. *Minerals* **2017**, *7*, 210. [[CrossRef](#)]
19. Umadevi, T.; Nelson, K.; Mahapatra, P.C.; Prabhu, M.; Ranjan, M. Influence of magnesia on iron ore sinter properties and productivity. *Ironmak. Steelmak.* **2009**, *36*, 515–520. [[CrossRef](#)]
20. Gan, Q.; He, Q.; Wen, Y. Study on influence of MgO on mineral composition and metallurgical properties of V-bearing titaniferous magnetite sinter. *Iron Steel* **2008**, *8*, 7–11.
21. Fan, X.H.; Li, W.Q.; Gan, M. Influence and mechanism of MgO on strength of high basicity sinter. *J. Cent. South Univ. (Sci. Technol.)* **2012**, *9*, 3325–3330.
22. Yang, S.T.; Zhou, M.; Jiang, T.; Wang, Y.J.; Xue, X.X. Effect of basicity on sintering behavior of low-titanium vanadium-titanium magnetite. *Trans. Nonferrous Met. Soc. China* **2015**, *25*, 2087–2094. [[CrossRef](#)]
23. Tang, W.D.; Yang, S.T.; Cheng, G.J.; Gao, Z.X.; Yang, H.; Xue, X.X. Effect of TiO<sub>2</sub> on the sintering behavior of chromium-bearing vanadium-titanium magnetite. *Minerals* **2018**, *8*, 263. [[CrossRef](#)]
24. Pelton, A.D. Thermodynamic database development—Modeling and phase diagram calculations in oxide systems. *Rare Met.* **2006**, *25*, 473–480. [[CrossRef](#)]
25. Trömel, G.; Koch, K.; Fix, W.; Großkurth, N. Magnesiumoxyds auf die gleichgewichte im system Fe–CaO–FeO–SiO<sub>2</sub> und auf die schwefelverteilung bei 1600 °C. *Archiv für das Eisenhüttenwesen* **1969**, *40*, 969–978. [[CrossRef](#)]
26. Panigrahy, S.; Verstraeten, P.; Dilewijns, J. Influence of MgO addition on mineralogy of iron ore sinter. *Metall. Mater. Trans. B* **1984**, *15*, 23–32. [[CrossRef](#)]
27. Long, H.; Yuan, X.; Liu, Z. *Iron Ore Powder Sintering Principle and Process*; Metallurgical Industry Press: Beijing, China, 2010.
28. Zhou, M.; Yang, S.; Jiang, T.; Xue, X. Influence of MgO in form of magnesite on properties and mineralogy of high chromium, vanadium, titanium magnetite sinters. *Ironmak. Steelmak.* **2015**, *42*, 217–225. [[CrossRef](#)]
29. Ma, J.Y.; Sun, X.W.; Sheng, S.X. Intensified smelting of vanadium and titanium magnetite in blast furnace. *Iron Steel (China)* **2000**, *35*, 4–8.
30. Qie, J.M.; Zhang, C.X.; Li, X.P.; Guo, Y.H.; Wang, H.F.; Wu, S.L. Lower SO<sub>2</sub> emissions in the sintering process utilizing the difference of sulphur contents of iron ores. *ISIJ Inter.* **2017**, *12*, 2115–2123. [[CrossRef](#)]

